1   **Revision 2**

2   **Local Structure Determination of Zn-smectite**

3   **QI TAO[1,2] *, CHAOGANG XING[3], SEUNGYEOL LEE[4,5], LONG YANG[6,7], QINGJIN**

4   **ZENG[1,8], SHANGYING LI[1], TIANQI ZHANG[1,8], GUANGLIE LV[3], HONGPING HE[1,2],**

5   **SRIDHAR KOMARNENI[9]****

6   [1] CAS Key Laboratory of Mineralogy and Metallogeny and Guangdong Provincial

7   Key Laboratory of Mineral Physics and Materials, Guangzhou Institute of

8   Geochemistry, Chinese Academy of Sciences, Guangzhou, 510640, P.R. China,

9   [2] CAS Center for Excellence in Deep Earth Science, Guangzhou, 510640, P.R. China,

10   [3] Analysis Center of Agrobiology and Environmental Sciences of Zhejiang

11   University, Hangzhou, 310058, P.R. China,

12   [4] USRA Lunar and Planetary Institute, 3600 Bay Area Boulevard, Houston, TX

13   77058, USA,

14   [5] ARES, NASA Johnson Space Center, 2101 NASA Parkway, Houston, TX 77058,

15   USA,

16   [6] Department of Applied Physics and Applied Mathematics, Columbia University,

17   New York, NY 10027, USA,

18   [7] School of Materials Science and Engineering, Tongji University, Shanghai 201804,

19   P.R. China

20   [8] University of Chinese Academy of Sciences, Beijing 100049, P.R. China,

21   [9] Department of Ecosystem Science and Management and Materials Research

22   Institute, 204 Energy and the Environment Laboratory, The Pennsylvania State

23   University, University Park, PA 16802, USA.

24   **Corresponding Authors**

25   **Qi Tao** - CAS Key Laboratory of Mineralogy and Metallogeny, Guangzhou Institute of

26   Geochemistry, Chinese Academy of Sciences, Guangzhou, 510640, P.R. China, ⓘ

27   orcid.org/0000-0003-3041-7299,

28   E-mail: taoqi@gig.ac.cn (Q.T.).

29   **Sridhar Komarneni** - Department of Ecosystem Science and Management and

30   Materials Research Institute, 204 Energy and the Environment Laboratory, The

31   Pennsylvania   State   University,   University   Park,   PA   16802,   USA, ⓘ

32   orcid.org/0000-0001-9102-1437

33   E-mail: sxk7@psu.edu (S.K.)

34

35 **ABSTRACT**

36   An aluminum-free zinc-bearing smectite (Zn-smectite) was synthesized under

37   hydrothermal conditions, together with its magnesium substituted products. Its layer

38   charges calculated by cation exchange capacity (CECs) is 117.4 mmol/100 g. X-ray

39   powder diffraction (XRD) results revealed turbostratic stacking and showed that the

40   d06l value of the Zn-smectite was > 1.525 Å, indicating that it is trioctahedral. Its

41   d001 value increased from *ca.*12.8 Å to *ca.* 16.0 Å after ethylene glycol (EG)

42   saturation. The Zn-smectite did not irreversibly collapse after heating the

43   Li^+-saturated sample to 300°C, suggesting that its layer charge was generated from

44   octahedral-site vacancies (defects). The Zn-smectite resembles zincsilite-like minerals

45   with interlayer Na^+ and Zn^{2+}. The intralayer structure of zincsilite was confirmed by

46   pair distribution function (PDF) analysis and the whole crystal structure was built and

47   optimized by DFT calculation in the CASTEP module of the Materials Studio

48   software. Synthetic zincsilite is triclinic, space group P –1 and its optimized unit-cell

49   parameters are: a=5.294 Å, b=9.162 Å, c=12.800 Å, α=90.788°, β=98.345° and

50   γ=90.399°.

51   **KEYWORDS:** Smectite, layer charge, local structure, turbostratic disorder, PDF

INTRODUCTION

52

53   Smectites are the most abundant group of clay minerals in Earth's near-surface

54   environments, and they therefore, play crucial roles in geological processes, such as

55   enrichment and migration of surface elements. Most smectites in soils and sediments

56   are formed by weathering transformation of micas to vermiculites to smectites and by

57   diagenetic and hydrothermal alteration of rocks (Hillier, 2003). Zinc-rich smectites

58   (Zn-smectites) are associated with supergene nonsulfide ores worldwide (Mondillo *et*

59   *al.*, 2015). Some of these are predominant economic minerals (*e.g.,* sauconite)

60   (Schingaro *et al.*, 2021) of the mineral assemblage derived by weathering (Newman

61   and Brown, 1987, Ross, 1946). As natural two-dimensional (2D) inorganic materials,

62   Zn-smectites have wide applications as catalysts and catalyst supports, luminescent

63   materials, adsorbents, *etc.* (Liu and Zhang, 2014, Wang *et al.*, 2019).

64   Zincsilite is a Zn containing but aluminum-free end-member of the

65   montmorillonite-zincsilite series (Smolianinova and Organoba, 1960), whose crystal

66   structure is far from well understood (Bergaya and Lagaly, 2013). At present, there

67   are relatively few studies on Zn-smectites synthesis (Ponce *et al.*, 2020, Vogels *et al.*,

68   2005, Zhou *et al.*, 2017), compared with saponite and hectorite of the same subgroup

69   (Kloprogge *et al.*, 1999). These studies were conducted mainly on synthetic

70   Zn-smectites prepared in the presence of Al (Ponce *et al.*, 2020, Vogels *et al.*, 2005,

71   Zhou *et al.*, 2017). There is no recording on the synthesis of such a mineral until 2008

72   (Petit *et al.*, 2008), although they considered their products to be sauconite-like

73 stevensite. The products were proposed to have a similar structural formulas with

74 stevensite, but with octahedral Zn instead of Mg, *i.e.*, $R_x^+Si_4(Zn_{3-x}\square_x)O_{10}(OH)_2$,

75 where R^+ and x are for interlayer cations and the number of octahedral vacancies,

76 respectively (Petit *et al.*, 2008). Apart from the results of Petit *et al.*, no reliable

77 unit-cell parameters and structural information are available for smectites of this

78 series (Anthony *et al.*, 2001). A lack of crystal structure information of these

79 smectites would limit their potential applications, for example, affecting the revelation

80 of the reaction mechanism when they are used as functional materials.

81   Refining the crystal structure of smectites is difficult, primarily because they lack

82 three-dimensionally (3D) order structures, and because of their fine grain size (usually

83 < 2 μm), and widespread layer stacking disorder (such as rotation and translational

84 shifts) (Meunier, 2006). Random rotations and translations within the *ab* plane

85 produce turbostratically disordered structures (Brindley and Brown, 1980, Moore and

86 Reymolds, 1997, Ufer *et al.*, 2004). In such cases, adjacent layers are no longer

87 optically coherent with each other, no orientation of the crystal can produce *hk0* (or

88 *hkl*) reflections from more than one layer (Brindley, and Brown, 1980, Moore and

89 Reymolds, 1997). For crystals containing successive turbostratic stacking layers,

90 asymmetric *hkl* reflections were obtained, as a characteristic of 2D crystals, similar to

91 those from a single layer (Lanson *et al.*, 2011, Ufer *et al.*, 2004). These types of

92 disorder make the common models insufficient to simulate the XRD profiles simply

93 by broadening Bragg reflections and the traditional Rietveld refinement completely

94   inappropriate to the structural determination and quantitative analysis of smectites

95   (Ufer *et al.*, 2004).

96   Computer programs were built to model the disordered layer structures of 2D

97   materials, such as DIFFaX (Braunbarth *et al.*, 2000, Hines *et al.*, 1997, Treacy *et al.*,

98   1991), DIFFaX+ (Leoni *et al.*, 2004), FAULTS (Casas-Cabanas *et al.*, 2016),

99   ROSS-X (Leonardi and Bish, 2020), *etc*. These programs have been used to model

100   diffraction from phyllosilicates, such as talc, kaolinites, illite, *etc.*, but have not for

101   smectites (Artioli *et al.*, 1995, Gualtieri, 1999, Gualtieri *et al.*, 2008, Viani *et al.*,

102   2002). It was until 2004 that Ufer *et al.* (2004, 2008) proposed a method (Ufer single

103   model) based upon the Debye formula (Debye, 1915, Yang and Frindt, 1996) for

104   modeling diffraction effects from smectites with turbostratic disorder within the

105   Rietveld method. Their models combined periodic/pseudoaperiodic calculations,

106   providing a successful and fast method for XRD profile simulation and phase

107   quantifications of smectites, as included in the BGMN program (Ufer *et al.*, 2004,

108   2008, 2012). With further development, structural features, such as layer charge

109   density and occupancies of octahedral sites of dioctahedral smectite had been

110   achieved using this method (Wang *et al.*, 2018). Although in the above cases, models

111   with special layer faults (such as used in DIFFaX+) or supper-cell (such as used in

112   single layer method) were used, the XRD patterns of smectites were successfully

113   simulated, however the crystal structure of smectite based on these simulation results

114   is still lacking, especially for the relevant atomic coordinates.

115   The atomic pair distribution function (PDF) method of analysis is a total

116   scattering technique, that gives the scaled probability $G(r)$ of finding two atoms in a

117   material at a distance r apart (Egami and Billinge, 2012, Neder and Proffen, 2008,

118   Young and Goodwin, 2011). It uses both the Bragg reflections and the diffuse

119   scattering (Lee and Xu, 2020). Therefore, it can be used to investigate not only a

120   long-range ordered structure, but also the short-range ordered local structure of a solid,

121   such as poorly ordered phases (*e.g.* nanocrystals and gels) and amorphous phases (*e.g.*

122   glasses and liquids) (Young and Goodwin, 2011, Juhas *et al.*,2010, Ojovan and

123   Louzguine-Luzgin, 2020, Schlesinger *et al.*, 2021). PDF analysis can reveal the

124   atomic structure from the total scattering data using the real-space refinement method

125   (Billinge and Kanatzidis, 2004, Lee and Xu, 2020). It is therefore, a promising

126   technique to determine the local structure of smectite.

127   In the present study, an aluminum-free zinc-bearing smectite (Zn-smectite), and

128   its magnesium substituted products (with varying molar ratios of octahedral

129   Zn^{2+}/Mg^{2+} cations) were synthesized under hydrothermal conditions. The resulting

130   materials were characterized by XRD, ^{29}Si solid-state magic-angle spinning nuclear

131   magnetic resonance spectroscopy (^{29}Si MAS NMR), and transmission electron

132   microscopy (TEM). Their layer charges were determined by their cation exchange

133   capacities (CECs). Based upon PDF analysis and refinement of the selected structural

134   models, the intralayer structure of the Zn-smectite was obtained using PDFgui

135   program (Farrow *et al.*, 2007). Subsequently, the overall structure of Zn-smectite

136   (including H in hydroxyl group and interlayer cations) was constructed by Materials

137   Studio software and optimized by DFT calculation. This is the first case to study the

138   local structure of Zn-smectite, and build its crystal structure with turbostratically

139   disordered layers based upon PDF analysis.

SAMPLES AND METHODS

Hydrothermal experiments

142   The synthesis for producing Zn-smectites used 10.23 g (0.036 mol)

143    $Na_2SiO_3·9H_2O$ (≥98.0%, Aladdin) and desired amounts of $ZnCl_2$ (≥98.0%,

144   Guangzhou Chemical Reagent Factory) and $MgCl_2·6H_2O$ (98.0%, Guangzhou

145   Chemical Reagent Factory), which were dissolved in 25 ml deionized (DI) water. 4.00

146   mol L^{-1} NaOH (≥96.0%, Guangzhou Chemical Reagent Factory) solution was added

147   to the above mixture while stirring until its pH reached *ca.* 10.00, which was

148   maintained for half an hour, and after the equilibration a uniform gel was eventually

149   obtained. The total volume of the mixtures was kept at 75 ml by adding DI water.

150   After that, the gel was transferred to a 100 ml Teflon-lined stain-less steel autoclave

151   and treated at 180°C for 48 h. The obtained precipitates were washed by several

152   centrifuge–washing cycles until the supernatant reached neutral pH followed by

153   drying at 65°C and grinding for further treatments. The amount of $ZnCl_2$ and

154    $MgCl_2·6H_2O$ were calculated by fixing the mole ratio of Si/M^{2+} as 3:2 per half unit

155   cell (p.h.u.c., $O_{10}(OH)_2$), in which M^{2+} represents the sum of the amounts of Zn^{2+} and

156   Mg^{2+} (in moles). This ratio was intentionally set to ensure that Si was sufficient for

157   the formation of a trioctahedral smectite structure (Si/M^{2+} = 4:3). The obtained

158   products were marked as S-Znx (x =1, 2, 3 and 4). For example, S-Zn1 represents the

159   sample synthesized with 6 moles of Si, 1 mole of Zn and 3 moles of Mg in the starting

160   chemicals.

161   The CECs of the synthesized samples were determined using the $[Co(NH_3)_6]^{3+}$

162   method (Bisio *et al.*, 2008). Briefly, a mixture of 500 mg synthetic samples and 30 ml

163   50 mmol L^{-1} $[Co(NH_3)_6]Cl$ (>99.0%, Aladdin) solution was shaken by a shaking table

164   at room temperature (*r.t.*) for 24 h to thoroughly exchange cations on the surfaces and

165   in the interlayers. After separation by centrifugation, the solution was analyzed by

166   UV–Vis spectrophotometry (UV-7504). The decrease in absorbance at 474 nm,

167   typical of the CT transition of $[Co(NH_3)_6]^{3+}$, was quantitatively related to the

168   difference in concentration by means of calibration with standard solutions. The

169   samples after $[Co(NH_3)_6]^{3+}$ exchange were designated as S-ZnxCo.

170   The Hofmann-Klemmen tests were done using the method described in the

171   literature (Petit *et al.*, 2008). Typically, 250 mg S-ZnxCo was put into a 50 ml

172   centrifuge tube with 30 ml 2.00 mol L^{-1} LiCl (≥97.0%, Sinopharm Chemical Regent)

173   solution. After sealing, the tube was shaken to thoroughly mix the solid and solution

174   using a shaking table for 2 h. After centrifugation, the supernatant solution was

175   removed, and the samples were shaken with another 30 ml 2.00 mol L^{-1} LiCl solution

176   for another 2 h. These treatments were repeated twice, and the mixing time was

177   extended to 24 h. After drying at 75°C, the products (expressed as S-ZnxLi) were

178   divided into two parts. One part was further heated at 300°C for 12 h (S-ZnxLi300).

179   **Analysis methodology**

180   **X-ray diffraction (XRD).** Powder XRD patterns were collected between 1° and

181   65° (2θ) at a scanning rate of 1° min^{-1} with a step size of 0.01° (2θ) and a fixed

182   divergence slit size of 0. 60° (2θ) on a Bruker D8 Advance diffractometer with

183   Ni-filtered Cu Kα radiation (λ=0.154 nm, 40 kV and 40 mA). The humidity is

184   controlled at *ca.* 30% by an automatic air dehumidifier. Randomly oriented samples

185   were prepared by pressing powder inside a cavity up to the reference level of the

186   sample holders. Oriented samples were prepared by pipetting the clay suspension onto

187   a glass slide and allowing it to dry at *r.t.* Glycolated samples were prepared by

188   treating the oriented samples in a desiccator with ethylene glycol (EG) at 30°C for 24

189   h.

190   **Fourier transform infrared (FTIR) spectroscopy.** FTIR spectra were obtained

191   by a Bruker VERTEX 70 Fourier transform infrared spectrometer, using KBr pressed

192   disk technique. 0.9 mg of each samples and 80 mg of KBr were well mixed and

193   ground in an agate mortar for 15 min. The mixtures were pressed for 5 min at 10

194   kbars and heated under a lamp for 3 min to remove adsorbed water before FTIR

195   measurements.. All spectra were collected at *r.t.* over the range of 400–4000 cm^{-1}

196   with a resolution of 4 cm^{-1} and 64 scans.

197   **Transmission electron microscopy (TEM).** TEM was performed with an FEI

198   Talos F200S field-emission transmission electron microscope, operating at an

199   accelerating voltage of 200 kV. Specimens were prepared by dispersing the sample in

200   ethanol and ultrasonically treating for 5 minutes. A drop of the resulting dispersion

201   was placed on a copper grid with carbon film coating, after which the ethanol was

202   evaporated.

203   To investigate the stacking structures of smectites along [001], oriented samples

204   were embedded in epoxy resin and dried at 100°C for 3 h. Subsequently, ultrathin

205   sections perpendicular to the film with a thickness of ~75 nm were sliced with a

206   diamond knife using a Lecia EM UC7 ultramicrotome. The thin sections were placed

207   on carbon-coated copper microgrids for TEM observations using the above

208   parameters.

209   **Magic-angle-spinning nuclear magnetic resonance spectroscopy (MAS**

210   **NMR).** ^{29}Si MAS NMR experiments were performed using a Bruker AVANCE III

211   600 spectrometer at resonance frequencies of 119.2 MHz. ^{29}Si MAS NMR spectra

212   with high-power proton decoupling were recorded on a 4 mm probe with a spinning

213   rate of 12 kHz, a π/4 pulse length of 2.6 µs, and a recycle delay of 80 s. The chemical

214   shifts of ^{29}Si were referenced to tetramethylsilane (TMS).

215   **Atomic pair distribution function (PDF) analysis and refinement.** X-ray total

216   scattering experiments for PDF analysis were carried out on a PANalytical Empyrean

217   Nano with an Ag source $K\alpha1$ (λ = 0.5594214 Å) and a GaliPIX 3D detector, at an

218   operating voltage of 60 kV and an operating current of 36 mA. All data were

219   collected at *r.t.* over an angular range (2θ) between 2° and 140°, with a step size of

220   0.0286°. Calibration of the experimental setup was done by measuring crystalline

221   silicon (NIST Si) as a standard material to calibrate the sample-to-detector distance

222   and to determine the Q_{damp} and Q_{broad}, which are the parameters that correct the PDF

223   envelope function for the instrument resolution (Egami and Billinge, 2012).

224   Diffraction data of empty polyimide tube were collected with the same exposure time

225   for background removal in the data reduction. The experimental data were converted

226   to PDF patterns using PDFgetX3 software (Juhas et al., 2013).

227   **Models refinement based upon PDF data and crystal structure optimization.**

228   PDF structural refinement were carried out using the PDFgui software (Farrow et al.,

229   2007). The initial models used to refine based upon PDF pattern of the Zn-sample

230   (S-Zn4) were with a C –1 and C2/m space group modified from talc (Drits et al., 2012)

231   and hectorite (Breu et al., 2003), respectively. Because X-ray diffraction is

232   comparatively insensitive in H as in -OH and the main focus of PDF local structure

233   modeling is the intra-layer structure, H and interlayer cations were removed from the

234   models. The structural formula for S-Zn4 model was calculated from chemical

235   composition determined by ICP-AES and the cation-exchange capacity. The fittings

236   using two models for S-Zn4 were performed between r_{min} =1 Å and r_{max} = 20 Å.

237   Unit-cell parameters, atomic site occupancies, atomic positions and atomic

238   displacement parameters (ADPs) were refined. The refined values Q_{damp} and Q_{broad}

239   were fixed in the subsequent structural refinements of the PDF data. The atomic

240   positions were fixed during the refinement of talc model (Drits et al., 2012), but were

241   refined with the hectorite model under the restrictions of the space group (Breu *et al.,*

242   2003).

243   After refinements, the unit-cell parameters, atomic coordinates and site

244   occupancies were input into the Materials Studio software package to further build the

245   overall crystal structure of Zn-smectite. The H as in –OH and interlayer cations were

246   restored, which were removed previously during the models refinement using PDF

247   data. The interlayer space was set to the d001 value from its XRD pattern. The H

248   atom was added to the octahedral O that was not connected to the tetrahedron with a

249   default O-H length (0.82 Å) and a direction paralleling to the layer stacking direction.

250   The number (p.h.u.c) and occupancy of interlayer cations were set according to the

251   corrected structural formula. Their initial atomic coordinates were set to the midpoint

252   of the two nearest –OH in the adjacent layers. Subsequently, the density functional

253   theory (DFT) based calculation was carried for the geometry optimization using

254   Perdew-Burke-Ernzerhof (PBE) function (Perdew et al., 1996), which is simplified by

255   generalized-gradient approximation (GGA) as in CASTEP module (Clark *et al.*, 2005).

256   A 3×2×1 k-points sampling grid was set for the optimization. The cutoff energy of the

257   projector augmented plane-wave basis was set at 598.7 eV to ensure energy accuracy.

258   The full geometry optimizations were carried out with convergence thresholds of

259   1.0×10^{-5} eV and 0.03 eV/Å for total energy and maximum force, respectively.

260   **RESULTS**

261   **XRD results of hydrothermal products**

262   XRD patterns of the synthetic samples showed a series of reflections at 2θ angles

263   *ca.* 5.84, 19.58, 28.78, 35.31, 59.70°, *etc.*, close to those of saponite (a Mg-rich

264   trioctahedral smectite) (Egami and Billinge, 2012) and other smectites (Figure 1)

265   (Faust *et al.*,1959, Petit *et al.*, 2008, Tao *et al.*, 2016). The *d* value of the *001*

266   reflection was *ca.* 12.8 Å for the S-Zn4 sample, which is a typical value of smectite

267   (Bergaya and Lagaly, 2013). All the other patterns in the range of 15 to 40° (2θ)

268   exhibit broad and asymmetric reflection maxima, typical of turbostratically stacked

269   smectites. Their *d* values of the diagnostic reflection *06l* band at *ca.* 60° (2θ) were all

270   larger than 1.525 Å, indicating that the samples are trioctahedral (Bergaya and Lagaly,

271   2013).

272

        Figure 1

273

274   With the increase in the Zn/Mg ratio, the relative intensity of the *001* reflection

275   was prominently increased, while the full width at half maximum (FWHM) decreased

276   from 6.44° (2θ) for S-Zn1 to 1.33° (2θ) for S-Zn4. The sample in which octahedral

277   sites were only occupied by Zn (Figure 1d) shows the narrowest and sharpest *001*

278   reflection with the highest intensity. After EG saturation, all samples except

279   S-Zn1_EG (Figure 2) showed increase in the relative intensity of the *001* reflections

280   (16.2 Å).

281

Figure 2

282 **^{29}Si MAS NMR Spectra of hydrothermal products**

283   The nearest neighbor environment of Si was assessed by ^{29}Si MAS NMR spectra.

284 Q^m (m =0, 1, 2, 3 and 4) was adopted to describe the Si environments in the solid

285 products, in which Q^m refers to the polymerization state of Si (Tao *et al.*, 2016). Two

286 main signals were recorded at *ca.* –95.0 and –83.8 ppm (Figure 3) for all the

287 as-synthesized samples, which are attributed to Q^3 Si and Q^2 Si, respectively. Signals

288 at *ca.* 110 ppm are ascribed to amorphous silica, as in all the samples except for

289 S-Zn4.

290

Figure 3

291

292 **TEM images of hydrothermal products**

293   Typical flaky grains with curled ribbon-like edges were observed in TEM images

294 for all products (Figure 4). This is a very common morphology for smectite minerals,

295 such as saponite and sauconite (Guven, 1988, Schingaro *et al.*, 2021, Tao *et al.*, 2019).

296 Among the products, S-Zn1 displayed the smallest particle sizes (Figure 4a). There

297 were loose fluffy needle-like fine grains randomly aggregated on its surface with a

298 thickness of several nanometers along the direction perpendicular to the crystal plates

299 (*c** direction). This is probably the lateral view of the particles, and they were

300 possibly formed by the curling of the very thin smectite layers. Similar aggregations

301   were also observed in S-Zn3 (Figure 4c). The S-Zn4 sample was readily identified

302   because it had the largest particle size (Figure 4d).

303

        Figure 4

304

305   Turbostratic layer stacking could be further evidenced by selected area electron

306   diffraction (SAED) of the samples. However, for such hydrated clay minerals, all

307   attempts to obtain its SAED failed due to the structural damage caused by the electron

308   beam under the vacuum of the TEM. Fortunately, lateral lattice images mostly along a

309   or b directions of the S-Zn4 grain were successfully obtained from ultrathin sections

310   of oriented samples embedded by epoxy (Figure 5). In the HRTEM image, the lateral

311   stacking of layers along the c direction could be clearly seen. The orientation could be

312   verified by the single layer distance (orange bar), which were calculated to be *ca.* 130

313   – 140 Å, close to 10 times of the d001 value of S-Zn4 (Figure 1). The fast Fourier

314   transform (FFT) of the HRTEM image were processed for the selected areas 1 and 2

315   (Figure 5). Although the diffraction spots were not clear, they still could be

316   recognized, which showed a ~ 12.5 Å d-spacing (Figures 5 and 2). This value was

317   also in accord with the d value as in XRD results (Figure 1). The turbostratic nature of

318   the crystal layer could be visually observed by the randomly distributed single layers

319   (orange arrow).

320

Figure 5

321

322 **DISCUSSIONS**

323 **Chemical compositions and origin of permanent layer charge**

324 Considering that ^{29}Si MAS NMR spectrum of S-Zn4 shows the least and

325 negligible amount of amorphous silica (Figure 3), its chemical composition and the

326 formula calculated from it are much closer to the pure phase than of all other products.

327 Therefore, elemental analysis of S-Zn4 and its Li^{+} exchanged product are selected and

328 measured by ICP-AES (Table 1), in which each value is the average of three parallel

329 tests. The synthesis of a pure sample with only Mg^{2+} in octahedral sites (stevensite)

330 turned out to be a XRD amorphous magnesium gel (not shown), which may require

331 much higher temperature and pressure to crystallize than those used in this study

332 (Golubeva *et al.*, 2005). The composition of S-Zn4 mainly consisted of silicon, zinc,

333 sodium and magnesium. Si always occupies tetrahedral sites in a smectite structure,

334 Zn and Mg generally occupy octahedral sites, and Na appear preferentially in the

335 interlayers. The calculation from chemical analyses showed that the total contents of

336 Zn was insufficient for the occupancy of all the octahedral sites (Schlesinger *et al.*,

337 2021). Some vacancies therefore must exist in the octahedral sheet to keep the ratio of

338 T/O at 4:3 and generate permanent layer charge. This kind of structure was commonly

339 found for ferric, nickel or magnesium trioctahedral smectites, which generates the

340 layer charge together with the effect of substitution in tetra- or/and octahedral sheets

341   from *ca.* 0.15e⁻ to 0.56e⁻ p.h.u.c. (Christidis and Mitsis, 2006, Hicks *et al.*, 2014,

342   Takahashi *et al.*, 1997, Vicente *et al.*, 1996).

343

        Table 1

344

345   Layer charge is an important characteristic of 2:1 smectites. It is not only a

346   criterion for the classification of smectites but also influences the capacity to retain

347   cations and to adsorb H_2O and polar organic molecules (Mermut *et al.*, 1994). The

348   layer charge of smectites arises primarily from the permanent charges generated by

349   isomorphous substitutions in their structure. Generally, both tetrahedral and

350   octahedral sheets can have these substitutions. For instance, in tetrahedral sheets,

351   there are often trivalent cation (typically Al^{3+}, Fe^{3+}) substitutions for Si^{4+}, whereas in

352   octahedral sheets, substitutions involve Mg^{2+}, Al^{3+}, Fe^{3+}, $Li^{+,}$ *etc.* (Lagaly, 2013). Two

353   types of octahedral substitutions generally occur. One involves the substitution of 3

354   bivalent cations by 2 trivalent cations and a vacancy ($3Mg^{2+} = 2Al^{3+} + \square$) (Kloprogge

355   *et al.*, 1994). The other is a one-to-one model, in which 1 Al^{3+} is replaced by 1 Mg^{2+}

356   (Suquet *et al.*, 1981). The former substitution has no effect on the layer charge,

357   whereas the latter generates a positive charge. In addition, there are also some special

358   smectites (*e.g..* stevensite), whose layer charge is generated by the presence of cation

359   deficiencies (vacancies) either in octahedral or tetrahedral sheets, or both, or even

360   with no cation substitution (Lagaly, 2013, Suquet *et al.*, 1981).

361   NMR spectra (Figure 3) showed that with increasing Zn/Mg, both Q^3 Si and Q^2

362   Si are intensified and increased in symmetry along with a decrease in peak width and

363   an increase in chemical shift (negative). Meanwhile, the intensity of the broad signals

364   at *ca.* −100 ppm decreased, corresponding to the gradual reduction of the amorphous

365   silica phase. If all three octahedral sites are occupied by Mg^{2+}, four Si^{4+} tetrahedra are

366   required p.h.u.c. to form the ideal 2:1 type of trioctahedral smectite structure (Si/Mg =

367   4:3). Considering that the concentration of Si was sufficient in the raw materials,

368   excess Si allowed the amorphous silica phase to precipitate in the products.   The

369   least and negligible amount of amorphous silica for S-Zn4 as shown by ^{29}Si MAS

370   NMR spectrum (Figure 3a) indicated that   most of input Si participated in the

371   formation of Zn-smectite. It requires more Zn than input to maintain the ideal T : O

372   ratio of 4:3 for a trioctahedral structure, which therefore leads to the possibility that

373   some cationic defects exist in the octahedral sheets of the zinciferous products, similar

374   to those in ZnO semiconductors (Fabbri *et al.*, 2014, Janotti and Van de walle, 2009,

375   Pan *et al.*, 2014). Actually, many elements, such as Mg, Fe, Ni etc., can form this kind

376   of octahedral vacancy with generated layer charge, similar to that in stevensite and

377   zincsilite, which can be deduced from the perspective of layer charge balance. The

378   -lowest amount of amorphous silica in S-Zn4 product compared with the other

379   products also implied that Zn is much easier to than Mg react with Si and crystallize

380   to form smectite with octahedral defects.

381   The layer charge of smectite was mainly contributed by permanent charge (Petit

382   *et al.*, 1995).   The CECs of all samples have been determined to estimate their layer

383   charge in this study (Table 2). All samples showed larger CECs (over 109 mmol/100

384   g) than those of typical dioctahedral smectites (*e.g.*, montmorillonite) and were

385   comparable with those of synthesized trioctahedral smectites (*e.g.*, saponite)

386   determined by the same processes (He *et al.*, 2014). The proportion of tetrahedra (T)

387   is 4 in p.h.u.c. for an ideal smectite. In this study, the input Si is excessive and there

388   are no other cations that can enter tetrahedra sites. Based upon the CEC value of

389   S-Zn4 and fixing the ratio of Si as 4 in p.h.u.c., the theoretical proportions of

390   interlayer cations (represent as Mi^+, *eg.* Nai^+), octahedral Zn and vacancies are

391   calculated as 0.58, 2.71 and 0.29, respectively. Therefore, the ideal structural formula

392   of S-Zn4 can be presented as $Zn_{0.27}Na_{0.04}(Zn_{2.71}\square_{0.29})Si_4O_{10}(OH)_{12}$ (Table 2).

393   According to the statistics in literature, there are usually at least 2.75 octahedral sites

394   should be occupied for the trioctahedral smectites, whose charges were generated by

395   isomorphic substitutions (Hutton, 1947). The number of occupied octahedral sites is

396   smaller than the value in this case, suggesting octahedral Zn defects existed. The

397   calculated layer charge p.h.u.c. (0.58) verified that the obtained product belongs to

398   high-charge trioctahedral smectites (0.48–0.60 e p.h.u.c.) (Christidis and Mitsis, 2006,

399   Milesi *et al.*, 2019).

400

      Table 2

401

402   It was also noticed that most of the interlayer cations are Zn^{2+} for S-Zn4 in this

403   case (Table 2). It was probably because there are no other cations available with the

404   exception of Na^+, during the formation of S-Zn4. This is obviously different from the

405   structure of sauconite, in which Zn is mainly located within the octahedral site, and

406   the Zn^{2+} adsorbed at the mineral surface or fixed in the interlayer is negligible or

407   lacking (Schingaro *et al.*, 2021).

408   **Layer charge position and its effects on the expandability of Zn-smectite:**

409   **Hoffmann-Klemen effects**

410   Previous research revealed that dioctahedral clay minerals saturated with small

411   cations such as Li^+ (ionic radius 0.90 Å) lose their cationic exchangeability after

412   heating at *ca.* 250°C for 24 h (Hofmann and Klemen, 1950). As there are ~1/3

413   unoccupied octahedral sites, the migration of Li^+ cations toward the vacant octahedral

414   sites appreciably reduces the octahedral layer charge. Migration of Li to the ditrigonal

415   cavities when heated is also a common phenomenon for dioctahedral smectites (*e.g.,*

416   beidellite), whose layer charges were generated only by tetrahedral substitutions

417   (Komadel *et al.*, 2005). In contrast, this effect does not occur in trioctahedral

418   smectites (*e.g.,* hectorite) (Glaeser and Mering, 1971).

419   In this case, there are *ca.* a total of 1/10 vacant octahedral sites for S-Zn4 (Table

420   2), and interlayer Li^+ can migrate to these sites during the heating treatment. Although,

421   the CEC value of the Li saturated sample is reduced to 27.13 mmol/100g, the heated

422   Li-bearing sample still shows an increased d001 value as 16.2 Å after in the XRD

423   pattern (Figure 6). This indicated that the adjacent TOT layers were not

424   "locked"/collapsed, demonstrating that the layer charge was generated by the

425   vacancies in the octahedral sites instead of isomorphic substitutions in tetrahedral

426   sheets.

427

Figure 6

428

429   After Li fixation, the Si–O–Si stretching bands become obviously narrower and

430   shifted to higher frequencies (up to 1019 cm^{-1}) than those of unheated samples (Figure

431   7). This trend is consistent with that for the reduced-charge montmorillonite

432   (Madejova et $al.$, 1996), reflecting the variation of magnitude and location of layer

433   charge (Kitajima et $al.$, 1991). Based upon all the results above, the products

434   synthesized in this case were determined to be zincsilite-like smectites.

435

Figure 7

436

437   **Characterization of the local structure of zincsilite by PDF analysis**

438   To obtain the crystal structure of S-Zn4, PDF analysis was applied because it is

439   very sensitive to short- and medium range-order. The decay of the PDF pattern for

440   S-Zn4 from low- to high-r regions suggested a ~24 Å coherent crystalline domain size

441   (intra-layer domain). The value is consistent with the height of $ca.$ 2 TOT layers

442   (Figure 1).

443   The PDF peaks represent interatomic distances in the material. The first peak at

444   ~1.58 Å corresponds to Si–O correlations in the tetrahedral sheet (Figures 8 and 9a′).

445   The second peak at ~2.16 Å is consistent with Zn–O correlations in the octahedral

446   sheet (Figures 8 and 9a′). The third peak at ~3.11 Å may consist of three kinds of

447   correlations, including the neighboring tetrahedral Si atoms that share a basal O, the

448   neighboring octahedral Zn atoms, and the adjacent apical O atoms that bridge

449   tetrahedral Si and octahedral Zn (Figures 8, and 9a′). The peak at ~5.39 Å, is

450   consistent with Si–Si correlations at the diagonal position in the interconnected six

451   membered SiO_4^{4-} rings, which may overlap with the correlations of the second nearest

452   Zn–Zn (Figures 8 and 9a′).

453

Figure 8

454

455   The selected models, *i.e.,* talc and hectorite have different symmetries. Talc has a

456   lower symmetry (C –1) than hectorite (C2/m). The refined results using talc as model

457   are almost in perfect fit with the experimental PDF data in the region of 1.0 to 20 Å

458   (Figures 9a and a′). The difference between the experimental and calculated patterns

459   reached as low as 0.037 (Rw) for *ca.* 10% vacancies random distributed in octahedral

460   sheet (Table 2 and Figure 9a). Although the calculated PDF pattern of modified

461   hectorite (interlayer cations removed) matched reasonably (Rw = 0.206) with the peak

462 positions of the experimental data (Figure 9b), obvious distortions could be clearly

463 observed by the mismatches in almost all peaks more or less (Figures 9b and b′). A

464 further check of the refined structure indicated that distorted bonds were generated

465 during the refinement processes, such as Si–O (Figures 9b and b′). These distortions

466 could also result from the Zn vacant sites, similar with those observed for layered

467 vernadite (Lee and Xu, 2020). They could further reduce the symmetry of phase,

468 which is probably the reason why talc model shows better match with the

469 experimental PDF pattern than that of hectorite framework.

470

Figure 9

471

472 To build the structure of zincsilite, the refined unit-cell parameters, atomic

473 coordinates and site occupancies using talc model were imported into Material Studio

474 software. The interlayer space was set to 12.800 Å according to XRD pattern (Figure

475 1). The H in hydroxyl groups was added to parallel with the layer stacking direction (c

476 directions). The amount of interlayer cations (1 for 4Si in p.h.u.c) and their

477 occupancies (0.58) were set according to the corrected structural formula. The initial

478 atomic coordinates of the interlayer cations were set to the midpoint of the two

479 adjacent hydroxyl groups in c^* direction. After optimization, the space group of the

480 crystal changes to P –1 and the cell parameters are as follows: a=5.294 Å, b=9.162 Å,

481 c=12.800 Å, α=90.788°, β=98.345° and γ=90.399° (Figure 10 and crystal structure

482   file in Supporting Materials).

483

    Figure 10

484

485   **CONCLUSION**

486   Obtaining the reliable crystal structure of smectite is very challenging by refining

487   of XRD reflections, because of its small crystallite size and the extensive stacking

488   disorder among the layers. In this study, zincsilite-like smectite has been successfully

489   synthesized, whose layer charge was generated by the Zn defects in octahedral sheets.

490   XRD and TEM results showed that turbostratically disordered layer stacking existed

491   in their grains. PDF analysis indicated that zincsilite only has a short-range order with

492   a domain size of *ca.* 24 Å (2 layers). Further refinement reveals that the structure of

493   the synthetic zincsilite fits talc with a triclinic symmetry better than hectorite with a

494   monoclinic. The lower symmetry of this zincsilite than the common smectite could be

495   attributed to its bond distortions in both tetrahedral and octahedral sheets, which

496   probably resulted from the octahedral Zn defects. Finally, the crystal structure of

497   zincsilite was built and optimized using DFT calculation in CASTEP module of

498   Materials Studio software with the unit-cell parameters obtained by talc model

499   refinement based upon PDF data, restoring interlayer cations and H atoms in hydroxyl

500   groups, and setting *c* value according to XRD results. The optimized structure is with

501   a P –1 space group and the unit-cell parameters are as follows: a=5.294 Å, b=9.162 Å,

502   c=12.800 Å, α=90.788°, β=98.345° and γ=90.399°.

503

504   **IMPLICATIONS**

505   Due to the variable composition, fine crystallite sizes, difficulty to synthesize

506   single crystal, as well as the widespread turbostratically disordered layers (Ufer *et al.*,

507   2004), XRD patterns of smectites contain no 3D information and therefore is

508   inapplicable to determine its crystal structure by traditional refinement method.

509   Meanwhile, as hydrated minerals with very fragile layers it is also very challenging to

510   obtain complete and reliable SAED patterns for crystal structure analysis. Although

511   smectite models can be constructed by XRD refinement, special techniques had to be

512   adopted to increase the layer stacking order, such as using F to replace –OH for

513   hectorite structure determination (Breu et al., 2003), otherwise the obtained model

514   actually represents merely the short-range ordered domains. How to directly, quickly,

515   and accurately obtain the crystal structure parameters and models of smectites has

516   been a continuous problem for decades.

517   This study reports a novel method to determine the crystal structure of smectite

518   by using a combination of the model refinement based upon PDF data and the

519   structure optimization by DFT calculation. Among them, PDF analysis provides

520   accurate the distance information between atoms using real-space refinement method

521   (Billinge and Kanatzidis, 2004, Lee and Xu, 2020), which does not depend on the

522   long-distance order of the structure (Egami and Billinge, 2012). Meanwhile, DFT

523   calculation can optimization of the positions of H atoms in –OH and interlayer cations.

524   Although zincsilite has more   octahedral defects than other common trioctahedral

525   smectite, the method is believed still effective for all smectites with both di- and tri-

526   octahedral structures, as well as the other materials and minerals with turbostratically

527   disordered layers, such as graphite, illite-smectites interstratified clay minerals *etc.*

528   (Neder and Proffen, 2008).

529   The CEC value shows that the amount of the charge reaches 117 mmol/100 g for

530   zincsilite, which is comparable with those of the common trioctahedral smectites (He

531   *et al.*, 2014). Because there is no substitution in either tetra- or octahedral sheets, and

532   its structure did not irreversibly collapse after heating the Li^+-saturated sample to

533   300°C (Hoffmann-Klemen effects),the layer charge of zincsilite is deduced as

534   generated   by   the   Zn   vacancies   (defects)   in   octahedral   sites.   Generally,

535   Hoffmann-Klemen   effect   is   much   common   for   dioctahedral   smectites   (such   as

536   beidellite) (Komadel *et al.*, 2005), while does not occur in trioctahedral smectite (such

537   as hectorite) (Glaeser and Mering, 1971). It is therefore inferred that expandability of

538   zincsilite with layer charge generated by octahedral vacancies is obviously different

539   from   common   trioctahedral   smectites,   whose   charge   generated   by   isomorphic

540   substitution, and similar with those in dioctahedral smectites.

541   Smectites   are   with   turbostratically   disordered   layers   along   stacking   direction,

542   which makes it impossible to build their 3-D crystal structure. However, their local

543   domain structures (such as intralayer structure) can be reliably determined by PDF

544   methods.

ACKNOWLEDGEMENT

554

FUNDING

ENDNOTE

560   Supplementary Information associated with this article can be found in the online

561   version.

REFERENCES CITED

563   Anthony, J. W. B., R.A., Bladh, K.W., Nichols, M.C. (2001) Handbook of
564   Mineralogy, Mineralogical Society of America: Chantilly.

565   Artioli, G., Bellotto, M., Gualtieri, A., Pavese, A. (1995) Nature of structural
566   disorder in natural kaolinites, a new model based on computer simulation of powder
567   diffraction data and electrostatic energy calculation. Clays and Clay Minerals, 43 (4),
568   438-445.

569   Bergaya, F., Lagaly, G. (2013) Handbook of Clay Science. 2nd ed., Elsevier:
570   Amsterdam, Netherlands.

571   Billinge, S.J.L., Kanatzidis, M.G. (2004) Beyond crystallography: the study of
572   disorder, nanocrystallinity and crystallographically challenged materials with pair
573   distribution functions. Chemical Communications, 35 (7), 749-760.

574   Bisio, C., Gatti, G., Boccaleri, E., Marchese, L., Superti, G.B., Pastore, H.O.,
575   Thommes, M. (2008) Understanding physico–chemical properties of saponite
576   synthetic clays. Microporous and Mesoporous Materials, 107 (1), 90-101.

577   Braunbarth, C., Hillhouse, H.W., Nair, S., Tsapatsis, M., Burton, A., Lobo, R.F.,
578   Jacubinas, R.M., Kuznicki, S.M. (2000) Structure of strontium ion-exchanged ETS-4
579   microporous molecular sieves. Chemistry of Materials, 12 (7), 1857-1865.

580   Brindley, G.W., Brown, G. (1980) Crystal structures of clay minerals and their
581   X-ray identification. In: Brindley, G.W., Brown, G. (Eds.), Mineral. Soc., London.

582   Breu, J., Seidl, W., Stoll, A. (2003) Fehlordnung bei smectiten in abhängigkeit
583   vom zwischenschichtkation. Zeitschrift fur Anorganische und Allgemeine Chemie,
584   629 (3), 503-515.

585   Casas-Cabanas, M., Reynaud, M., Rikarte, J., Horbach, P., Rodríguez-Carvajal, J.
586   (2016) FAULTS: a program for refinement of structures with extended defects.
587   Journal of Applied Crystallography, 49, 2259-2269.

588   Christidis, G.E., Mitsis, I. (2006) A New Ni-rich stevensite from the ophiolite
589   complex of Othrys, central Greece. Clays and Clay Minerals, 54 (6), 653-666.

590   Clark, S.J., Segall, M.D., Pickard, C.J., Hasnip, P.J., Probert, M.I.J., Refson, K.,
591   Payne, M.C. (2005) First principles methods using CASTEP. Zeitschrift fur
592   Kristallographie-Crystalline Materials, 220 (5-6), 567-570.

593   Debye, P. (1915) Zerstreuung von röntgenstrahlen. Annalen Der Physik, 351 (6),
594   809-823.

595   Drits, V.A., Guggenheim, S., Zviagina, B.B., Kogure, T. (2012) Structures of the
596   2:1 layers of pyrophyllite and talc. Clays and Clay Minerals, 60 (6), 574-587.

597   Egami, T., Billinge, S. J.L. (2012) Underneath the Bragg Peaks: Structural
598   Analysis of Complex Materials. Elsevier: Amsterdam, Vol. 16.

599   Fabbri, F., Villani, M., Catellani, A., Calzolari, A., Cicero, G., Calestani, D.,
600   Calestani, G., Zappettini, A., Dierre, B., Sekiguchi, T., Salviati, G. (2014) Zn vacancy
601   induced green luminescence on non-polar surfaces in ZnO nanostructures. Scientific
602   Reports, 4 (1), 5158.

603   Farrow, C.L., Juhas, P., Liu, J.W., Bryndin, D., Božin, E. S., Bloch, J., Proffen,
604   T., Billinge, S.J. (2007) PDFfit2 and PDFgui: computer programs for studying
605   nanostructure in crystals. Journal of Physics: Condensed Matter, 19 (33), 335219.

606   Faust, G.T., Hathaway, J.C., Millot, G. (1959) A restudy of stevensite and allied
607   minerals. American Mineralogist, 44, 342-370.

608   Glaeser, R., Mering, J. (1971) Migration of Li cations in dioctahedral smectites
609   (Hofmann-Klemen effect). Comptes Rendus Hebdomadaires des Séances de l Acadé
610   mie des Sciences. D: Sciences Naturelles, 273 (25), 2399-2402.

611   Golubeva, O.Yu., Korytkova, E.N., Gusarov, V.V. (2005) Hydrothermal
612   synthesis of magnesium silicate montmorillonite for polymer-clay nanocomposites.
613   Russian Journal of Applied Chemistry, 78(1), 26-32.

614   Grauby, O., Petit, S., Decarreau, A., Baronnet, A. (1993) The beidellite-saponite
615   series, an experimental approach. European Journal of Mineralogy, 5 (4), 623-635.

616   Gualtieri, A.F. (1999) Modelling the nature of disorder in talc by simulation of
617   X-ray powder patterns. European Journal of Mineralogy, 11 (3), 521-532.

618   Gualtieri, A.F., Ferrari, S., Leoni, M., Grathoff, G., Hugo, R., Shatnawi, M.,
619   Paglia, G., Billinge, S. (2008) Structural characterization of the clay mineral illite-1M.
620   Journal of Applied Crystallography, 41 (2), 402-415.

621   Guven, N. (1988) Smectites. Reviews in Mineralogy and Geochemistry, 19 (1),
622   497–559.

623   He, H., Li, T., T ao, Q., Chen, T., Zhang, D., Zhu, J., Yuan, P., Zhu, R. (2014)
624   Aluminum ion occupancy in the structure of synthetic saponites: Effect on
625   crystallinity. American Mineralogists, 99 (1), 109-116.

626   Hicks, L.J., Bridges, J.C., Gurman, S.J. (2014) Ferric saponite and serpentine in
627   the nakhlite martian meteorites. Geochimica et Cosmochimica Acta, 136, 194-210.

628   Hillier, S. (2003) In *Encyclopedia of Sediments and Sedimentary Rocks*,
629   Middleton, G. V., Church, M. J., Coniglio, M., Hardie, L. A., Longstaffe, F. J., Ed.,
630   Springer Netherlands: Dordrecht, pp 139-142.

631   Hines, D.R., Seidler, G.T., Treacy, M.M.J., Solin, S.A. (1997) Random stacking
632   of a commensurate guest layer in an ordered host: NiAl layer-double-hydroxides.
633   Solid State Communications, 101 (11), 835-839.

634   Hofmann, U., Klemen, R. (1950) Verlust der austauschfähigkeit von lithiumionen

635   an bentonit durch erhitzung. Zeitschrift für Anorganische und Allgemeine Chemie,
636   262 (1-5), 95–99.

637   Hutton, C.O. (1947) Contribution to the mineralogy of the New Zealand, part 3.
638   Transactions of the Royal Society of New Zealand, 76, 481-491.

639   Janotti, A., Van de Walle, C.G. (2009) Fundamentals of zinc oxide as a
640   semiconductor. Reports on Progress in Physics, 72 (12), 126501.

641   Juhas, P., Davis, T., Farrow, C.L., Billinge, S.J.L. (2013) PDFgetX3: a rapid and
642   highly automatable program for processing powder diffraction data into total
643   scattering pair distribution functions. Journal of Applied Crystallography, 46,
644   560-566.

645   Juhas, P., Granlund, L., Gujarathi, S.R., Duxbury, P.M., Billinge, S.J.L. (2010)
646   Crystal structure solution from experimentally determined atomic pair distribution
647   functions. Journal of Applied Crystallography, 43 (3), 623-629.

648   Kitajima, K., Taruta, S., Takusagawa, N. (1991) Effects of layer charge on the IR
649   spectra of synthetic fluorine micas. Clay Minerals, 26 (3), 435-440.

650   Kloprogge, J.T., Breukelaar, J., Geus, J.W., Jansen, J.B.H. (1994)
651   Characterization of Mg-saponites synthesized from gels containing amounts of Na^+,
652   K^+, Rb^+, Ca^{2+}, Ba^{2+}, or Ce^{4+} equivalent to the CEC of the saponite. Clays and Clay
653   Minerals, 42 (1), 18-22.

654   Kloprogge, J.T., Komarneni, S., Amonette, J. (1999) Synthesis of smectite clay
655   minerals: a critical review. Clays and Clay Minerals, 47, 529-554.

656   Komadel, P., Madejova, J., Bujdak, J. (2005) Preparation and properties of
657   reduced-charge smectites - A review. Clays and Clay Minerals, 53 (4), 313-334.

658   Lanson, B., Brigatti, M.F., Mottana, A. (2011) In *Layered Mineral Structures and*
659   *their Application in Advanced Technologies*, Mineralogical Society of Great Britain
660   and Ireland, Chapter 4, Vol. 11, pp 151-202.

661   Lee, S., Xu, H. (2020) Using complementary methods of synchrotron radiation
662   powder diffraction and pair distribution function to refine crystal structures with high
663   quality parameters-A review. Minerals, 10 (2), 124.

664   Leonardi, A., Bish, D.L. (2020) Understanding powder x-ray diffraction profiles
665   from layered minerals: The case of kaolinite nanocrystals. Inorganic Chemistry, 59
666   (8), 5357-5367.

667   Leoni, M., Gualtieri, A. F., Roveri, N. Simultaneous refinement of structure and
668   microstructure of layered materials. Journal of Applied Crystallography, 37 (1),
669   166-173.

670   Liu, J., Zhang, G. (2014) Recent advances in synthesis and applications of

671   clay-based photocatalysts: a review. Physical Chemistry Chemical Physics, 16 (18),
672   8178-8192.

673   Lutterotti, L. (2010) Total pattern fitting for the combined size–strain–stress–
674   texture determination in thin film diffraction. Nuclear Instruments & Methods In
675   Physics Research Section B-beam Interactions With Materials And Atoms, 268 (3),
676   334-340.

677   Madejova, J., Bujdak, J., Gates, W.P., Komadel, P. (1996) Preparation and
678   infrared spectroscopic characterization of reduced-charge montmorillonite with
679   various Li contents. Clay Minerals, 31 (2), 233-241.

680   Mermut, A.R., Boyd, S.A., Farmer, W.J., Jaynes, W.F., Lagaly, G., Laird, D.A.,
681   Mermut, A.R. (1994) *Layer Charge Characteristics of 2:1 Silicate Clay Minerals*.
682   Clay Minerals Society, Evergreen.

683   Meunier, A. (2006) Why are clay minerals small? Clay Minerals, 41 (2),
684   551-566.

685   Milesi, V. P., Jézéquel, D., Debure, M., Cadeau, P., Guyot, F., Sarazin, G., Claret,
686   F., Vennin, E., Chaduteau, C., Virgone, A., Gaucher, E. C., Ader, M. (2019)
687   Formation of magnesium-smectite during lacustrine carbonates early diagenesis:
688   Study case of the volcanic crater lake Dziani Dzaha (Mayotte – Indian Ocean).
689   Sedimentology, 66 (3), 983-1001.

690   Mondillo, N., Nieto, F., Balassone, G. (2015) Micro- and nano-characterization
691   of Zn-clays in nonsulfide supergene ores of southern Peru. American MIneralogists,
692   100 (11-12), 2484-2496.

693   Moore, D.M., Reynolds Jr., R.C., (1997) *X-ray Diffraction and the Identification*
694   *and Analysis of Clay Minerals*, 2nd ed. Oxford University Press, New York, pp. 335–
695   339.

696   Neder, R. B., Proffen, T. (2008) Diffuse Scattering and Defect Structure
697   Simulations: A Cook Book Using the Program DISCUS. Oxford University Press Inc.:
698   Online.

699   Newman, A., Brown, G. (1987) The chemical constitution of clays. A.C.D.
700   Newman (Ed.), Chemistry of clays and clay minerals, Mineralogical Society
701   Monograph No. 6, John Wiley & sons, New York.

702   Ojovan, M.I., Louzguine-Luzgin, D.V. (2020) Revealing structural changes at
703   glass transition via radial distribution functions. Journal of Physical Chemistry B, 124
704   (15), 3186-3194.

705   Pan, L., Wang, S., Mi, W., Song, J., Zou, J.-J., Wang, L., Zhang, X. (2014)
706   Undoped ZnO abundant with metal vacancies. Nano Energy, 9, 71-79.

707   Perdew, J.P., Burke, K., Ernzerhof, M. (1996) Generalized gradient
708   approximation made simple. Physical Revview Letters, 77, 3865-3868.

709   Petit, S., Decarreau, A., Mosser, C., Ehret, G., Grauby, O. (1995) Hydrothermal
710   synthesis (250°C) of copper-substituted kaolinites. Clays and Clay Minerals, 43 (4),
711   482-494.

712   Petit, S., Righi, D., Decarreau, A. (2008) Transformation of synthetic
713   Zn-stevensite to Zn-talc induced by the Hofmann-Klemen effect. Clays and Clay
714   Minerals, 56 (6), 645-654.

715   Ponce, C.P., Kloprogge, J.T. (2020) Urea-assisted synthesis and characterization
716   of saponite with different octahedral (Mg, Zn, Ni, Co) and tetrahedral metals (Al, Ga,
717   B), a review. Life, 10, 168-.

718   Ross, C. S. (1946) Sauconite-a clay mineral of the montmorillonite Group.
719   American Mineralogists, 31 (9-10), 411-424.

720   Schingaro, E., Ventruti, G., Vinci, D., Balassone, G., Mondillo, N., Nieto, F.,
721   Lacalamita, M., Leoni, M. (2021) New insights into the crystal chemistry of sauconite
722   (Zn-smectite) from the Skorpion zinc deposit (Namibia) via a multi-methodological
723   approach. American Mineralogists, 106 (2), 290-300.

724   Schlesinger, C., Habermehl, S., Prill, D. (2021) Structure determination of
725   organic compounds by a fit to the pair distribution function from scratch without prior
726   indexing. Journal of Applied Crystallography, 54, 776-786.

727   Smolianinova, N. N. M., V.A., Organoba, N.I., (1960) New aluminum-free
728   member of the montmorillonite-sauconite series. In Acad. Sci. URSS, Commission
729   for Study of Clays, Report to Meeting of International Commission for Study of Clays,
730   pp 45-52.

731   Suquet, H., Malard, C., Copin, E., Pezerat, H. (1981) Variation du parametre b et
732   de la distance basale dool dans une serie de saponites a charge croissante: ii. etats zero
733   couche. Clay Minerals, 16 (2), 181-193.

734   Takahashi, N., Tanaka, M., Satoh, T., Endo, T., Shimada, M. (1997) Study of
735   synthetic clay minerals. Part IV: synthesis of microcrystalline stevensite from
736   hydromagnesite and sodium silicate. Microporous Materials, 9 (1), 35-42.

737   Tao, Q., Fang, Y., Li, T., Zhang, D., Chen, M., Ji, S., He, H., (2016) Komarneni,
738   S., Zhang, H., Dong, Y., Noh, Y. D. Silylation of saponite with
739   3-aminopropyltriethoxysilane. Applied Clay Sciences, 132, 133-139.

740   Tao, Q., Zeng, Q., Chen, M., He, H., Komarneni, S. (2019) Formation of saponite
741   by hydrothermal alteration of metal oxides: Implication for the rarity of hydrotalcite.
742   American Mineralogists, 104 (8), 1156-1164.

743   Treacy, M. M. J., Newsam, J. M., Deem, M. W. (1991) A general recursion
744   method for calculating diffracted intensities from crystals containing planar faults.
745   Proceedings of the Royal Society of London A: Mathematical, 433(1889), 499-520.

746   Ufer, K., Kleeberg, R., Bergmann, J., Dohrmann, R. Rietveld refinement of
747   disordered illite-smectite mixed-layer structures by a recursive algorithm. II:
748   powder-pattern refinement and quantitative phase analysis. Clays and Clay Minerals,
749   60 (5), 535-552.

750   Ufer, K., Roth, G., Kleeberg, R., Stanjek, H., Dohrmann, R., Bergmann, J. (2004)
751   Description of X-ray powder pattern of turbostratically disordered layer structures
752   with a Rietveld compatible approach. Zeitschrift fur Kristallographie, 219 (9),
753   519-527.

754   Ufer, K., Stanjek, H., Roth, G., Dohrmann, R., Kleeberg, R., Kaufhold, S. (2008)
755   Quantitative phase analysis of bentonites by the Rietveld method. Clays and Clay
756   Minerals, 56 (2), 272-282.

757   Ufer, K., Kleeberg, R., Bergmann, J., Dohrmann, R. (2012) Rietveld refinement
758   of disordered illite-smectite mixed-layer structures by a recursive algorithm. II:
759   Powder-pattern refinement and quantitative phase analysis. Clays and Clay Minerals,
760   60 (5), 535-552.

761   Viani, A., Gualtieri, A. F., Artioli, G. (2002) The nature of disorder in
762   montmorillonite by simulation of X-ray powder patterns. American Mineralogists, 87
763   (7), 966-975.

764   Vicente, M.A., Suárez, M., López-González, J.d.D., Bañares-Muñoz, M.A. (1996)
765   Characterization, surface area, and porosity analyses of the solids obtained by acid
766   leaching of a saponite. Langmuir, 12 (2), 566-572.

767   Vogels, R.J.M.J., Kloprogge, J.T., Geus, J.W. (2005) Synthesis and
768   characterization of saponite clays. American Mineralogists, 90(5-6), 931–944.

769   Wang, L., Bahnemann, D. W., Bian, L., Dong, G., Zhao, J., Wang, C. (2019)
770   Two-dimensional layered zinc silicate nanosheets with excellent photocatalytic
771   performance for organic pollutant degradation and CO_2 conversion. Angewandte
772   Chemie International Edition, 58 (24), 8103-8108.

773   Wang, X., Ufer, K., Kleeberg, R. (2018) Routine investigation of structural
774   parameters of dioctahedral smectites by the Rietveld method. Applied Clay Sciences,
775   163, 257-264.

776   Yang, D., Frindt, R.F. (1996) Powder X-ray diffraction of turbostratically stacked
777   layer systems. Journal of Materials Research, 11 (7), 1733-1738.

778   Young, C. A., Goodwin, A. L. (2011) Applications of pair distribution function
779   methods to contemporary problems in materials chemistry. Journal of Materials

780   Chemistry, 21 (18), 6464-6476.

781   Zhang, C., He, H., Tao, Q., Ji, S., Li, S., Ma, L., Su, X., Zhu, J. (2016) Metal
782   occupancy and its influence on thermal stability of synthetic saponites. Applied Clay
783   Sciences, 135, 282-288.

784   Zhou, R., Basu, K., Hartman, H., Matocha, C.J., Sears, S.K., Vali, H., Guzman,
785   M.I. (2017) Catalyzed Synthesis of Zinc Clays by Prebiotic Central Metabolites.
786   Scientific Reports. 2017, 7, 533.

787

788   **LIST OF TABLES**

789   **Table 1.** The chemical compositions (wt%) by ICP-AES of the products

Samples	SiO_2	ZnO	Na_2O	Li_2O	Else[#]	L.O.I.	Total (%)
S-Zn4	49.70	41.30	0.67	–	0.14	7.13	98.94
S-Zn4-Li	49.40	40.90	0.05	0.23	0.17	8.09	98.84

[#] "Else" includes those are not intended to input as source chemicals and with trace amount of contents, including Ca, Fe, Al, Ti, *etc.*

790

791   **Table 2.** CECs and calculated structural formulas of as-synthesized samples
792

Samples	CECs (mmol/100 g)	Structural Formulas	
		Calculated by CECs[§]	Corrected by compositions
S-Zn1	115.7	$Mi_{0.58}{}^{[‡]}[(Zn,Mg)_{2.71}\square_{0.29}]Si_4O_{10}(OH)_2$	N.D.
S-Zn2	109.5	$Mi_{0.54}[(Zn,Mg)_{2.73}\square_{0.27}]Si_4O_{10}(OH)_2$	N.D.
S-Zn3	114.4	$Mi_{0.57}[(Zn,Mg)_{2.72}\square_{0.28}]Si_4O_{10}(OH)_2$	N.D.
S-Zn4	117.4	$Mi_{0.58}(Zn_{2.71}\square_{0.29})Si_4O_{10}(OH)_2$	$Zn_{0.27}Na_{0.04}(Zn_{2.71}\square_{0.29})Si_4O_{10}(OH)_2$

793   [§] Calculation method: The proportion of Si (excessive) p.h.u.c. was set to 4.

794   [‡] Mi represents the interlayer cation

795   N.D. represents Not Determined.

796

797

798   **FIGURE CAPTIONS**

799   Figure 1 XRD patterns of the samples with different concentrations of Zn and Mg in

800   octahedral sheet. a. S-Zn1, b. S-Zn2, c. S-Zn3 and d. S-Zn4.

801   Figure 2 XRD patterns of EG saturated samples: a. S-Zn1EG, b. S-Zn2EG, c.

802   S-Zn3EG, and d. S-Zn4EG.

803   Figure 3 ^{29}Si MAS NMR spectra of synthesized samples: a. S-Zn1, b. S-Zn2, c. S-Zn3,

804   and d. S-Zn4.

805   Figure 4 TEM images of synthesized samples: a. S-Zn1, b. S-Zn2, c. S-Zn3 and d.

806   S-Zn4.

807   Figure 5 HRTEM image of the ultrathin section of S-Zn4 with the turbostratically

808   disordered layers.

809   L represents the thickness of a layer. The arrows indicate the areas where the layers

810   are stacked in random orientations.

811   Figure 6 XRD patterns of the EG saturated samples after H-K effect tests.

812   Figure 7 FTIR spectra of Co exchanged samples (after CECs tests), Li exchanged

813   samples, and 300°C heated Li exchanged samples.

814   a. S-Zn1Co, b. S-Zn1Li, c. S-Zn1Li300, d. S-Zn2Co, e. S-Zn2Li, f. S-Zn2Li300, g.

815   S-Zn3Co, h. S-Zn3-Li, i. S-Zn3Li300, j. S-Zn4Co, k. S-Zn4-Li, and l. S-Zn4Li300.

816   Figure 8 The experimental PDF data of S-Zn4 from 1 Å to 40 Å range. The decay of

817   the pattern suggests a ~24 Å coherent crystalline domain.

818   Figure 9 PDF patterns of S-Zn4 from 1 to 20 Å range and related refinements using

819   different models: a. Talc with a triclinic symmetry and a C –1 space group. b.

820   Hectorite with a monoclinic symmetry and a C2/m space group. a′ and b′ show the

821   interatomic distances in the resulted structures.

822   Figure 10 The front (a and a′), side (b and b′) and top (c and c′) views of optimized

823   crystal structure of zincsilite. The octahedra and atoms in blue represent octahedral Zn

824   defects.

825
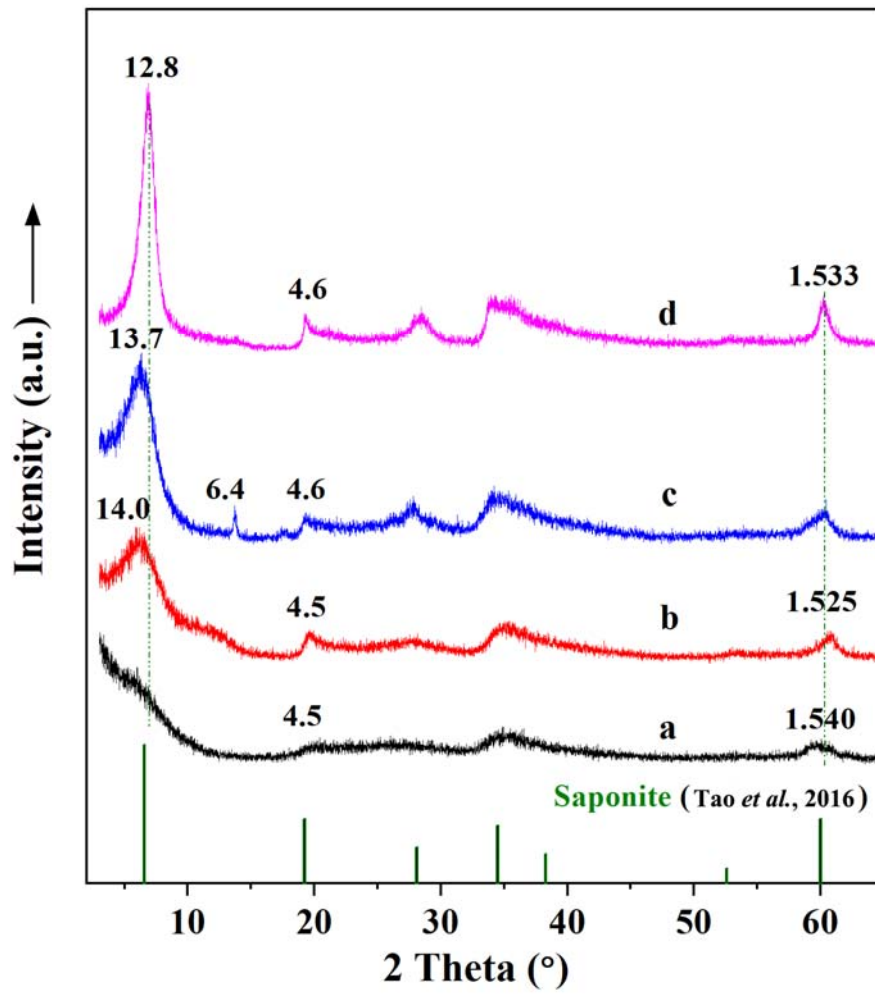
826

827   Figure 1

828
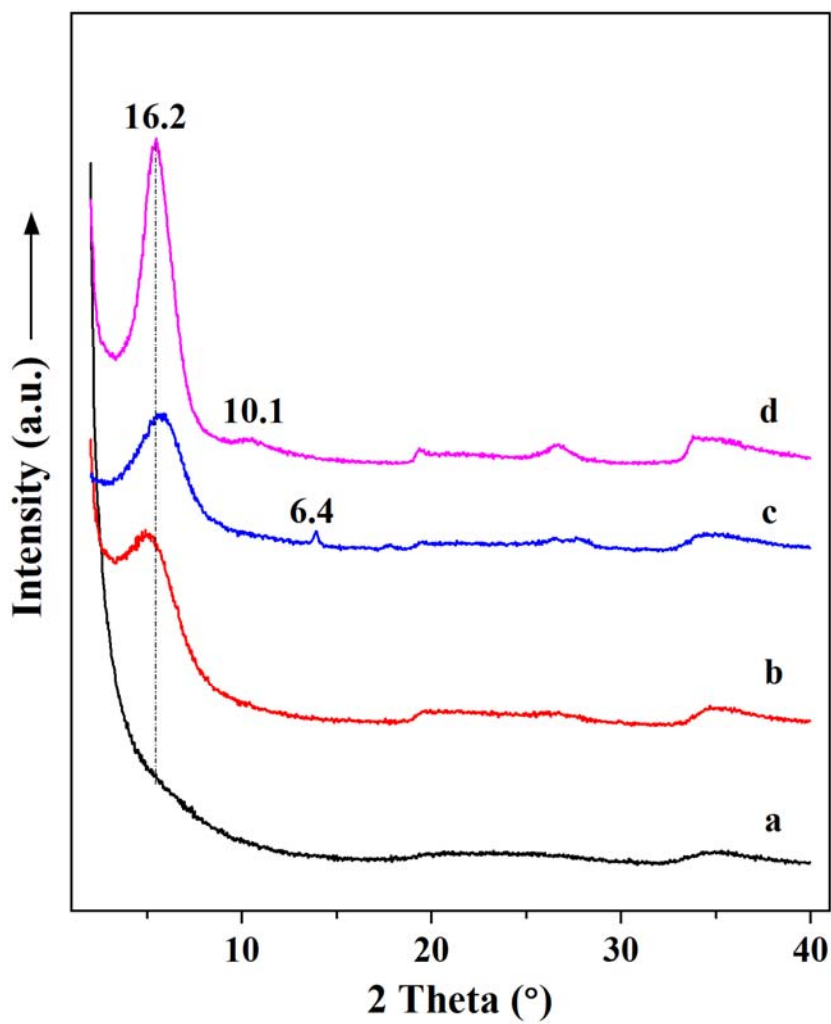
829

830 Figure 2
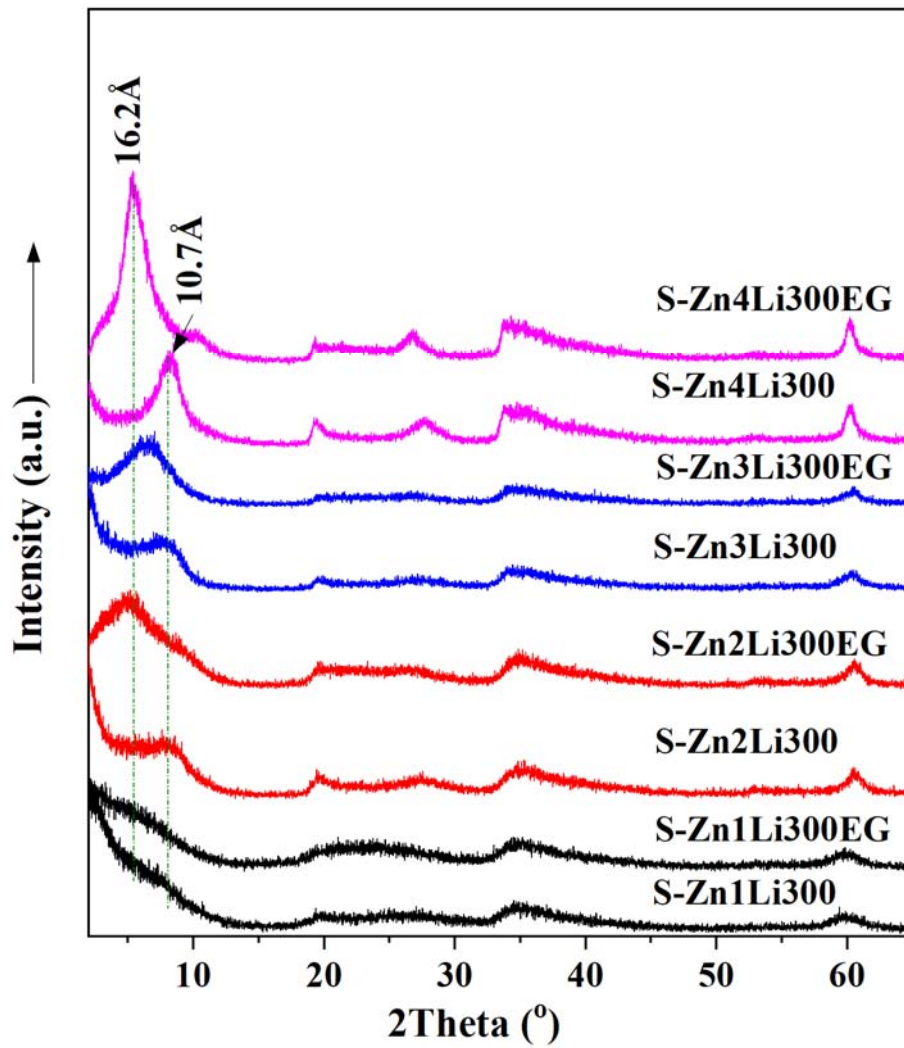
831

832
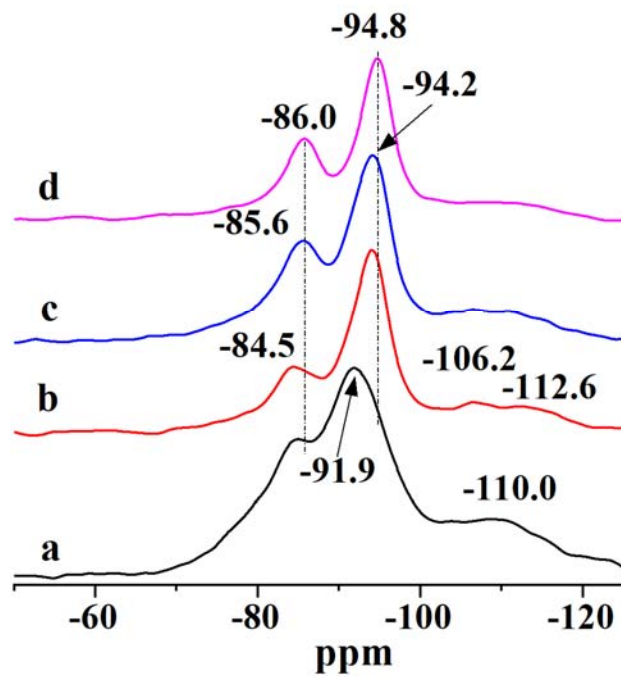
833

834   Figure 3
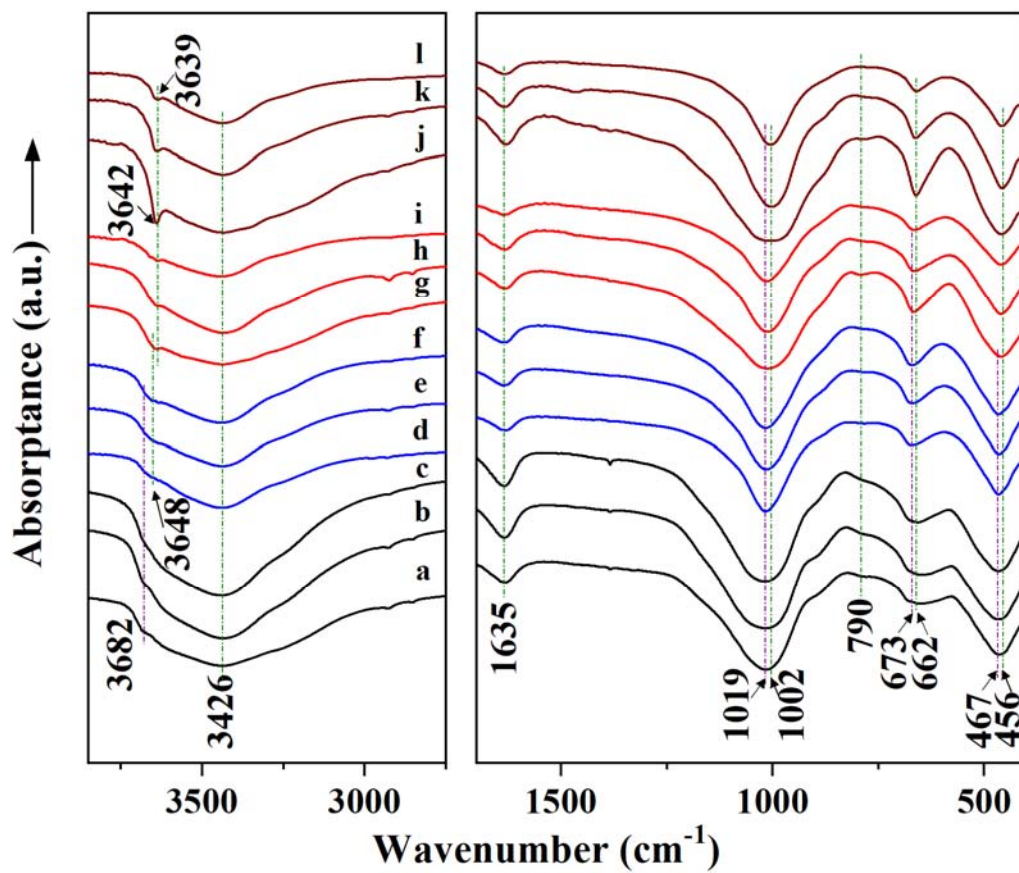
835
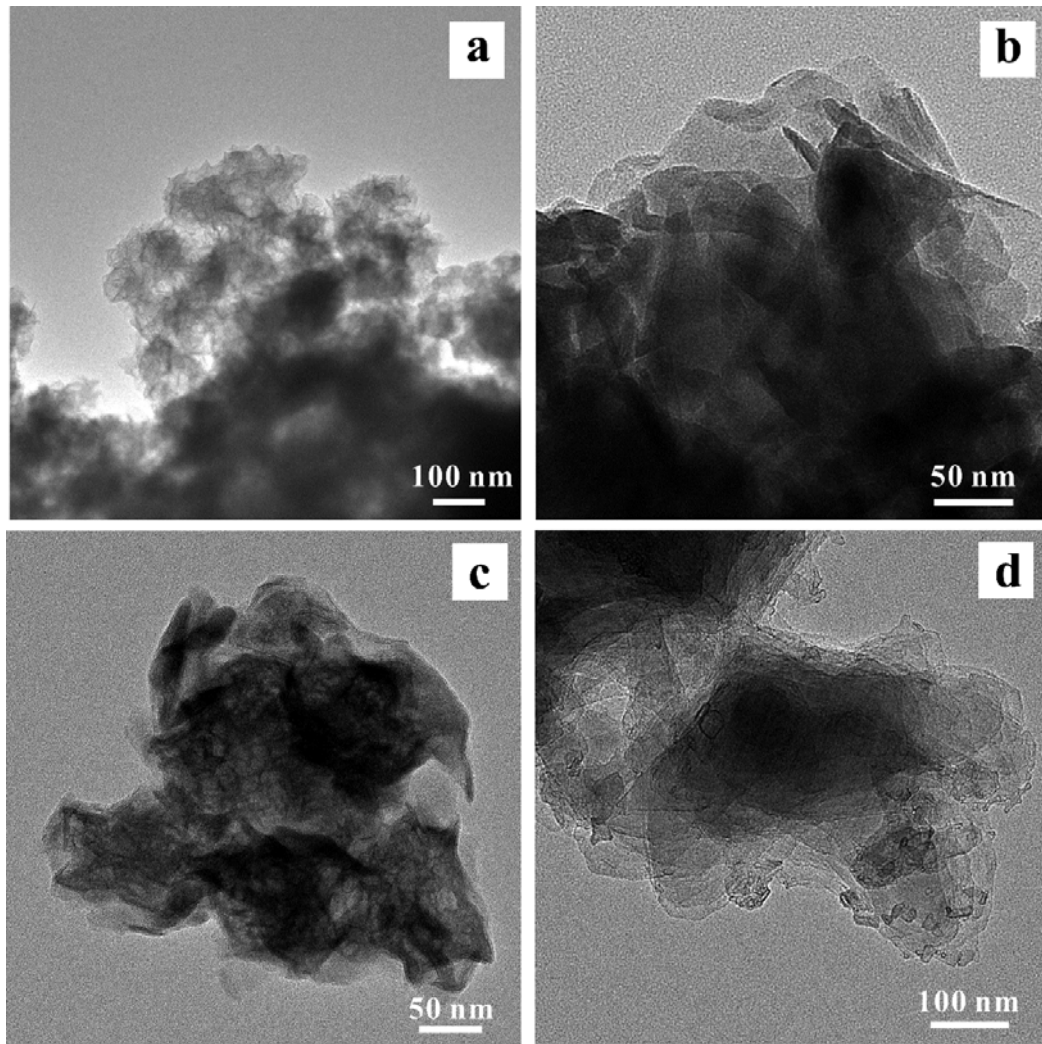
836

837 Figure 4

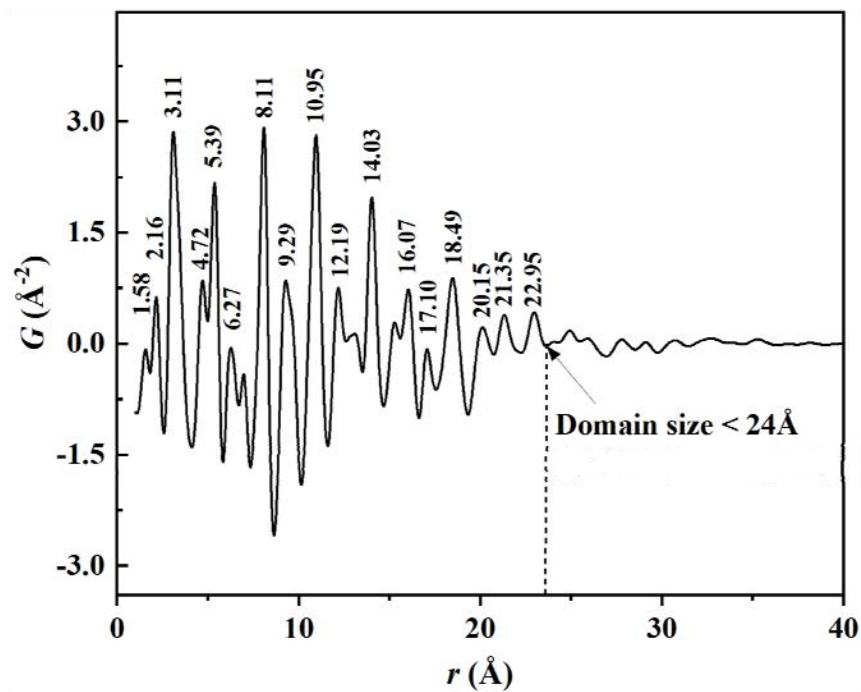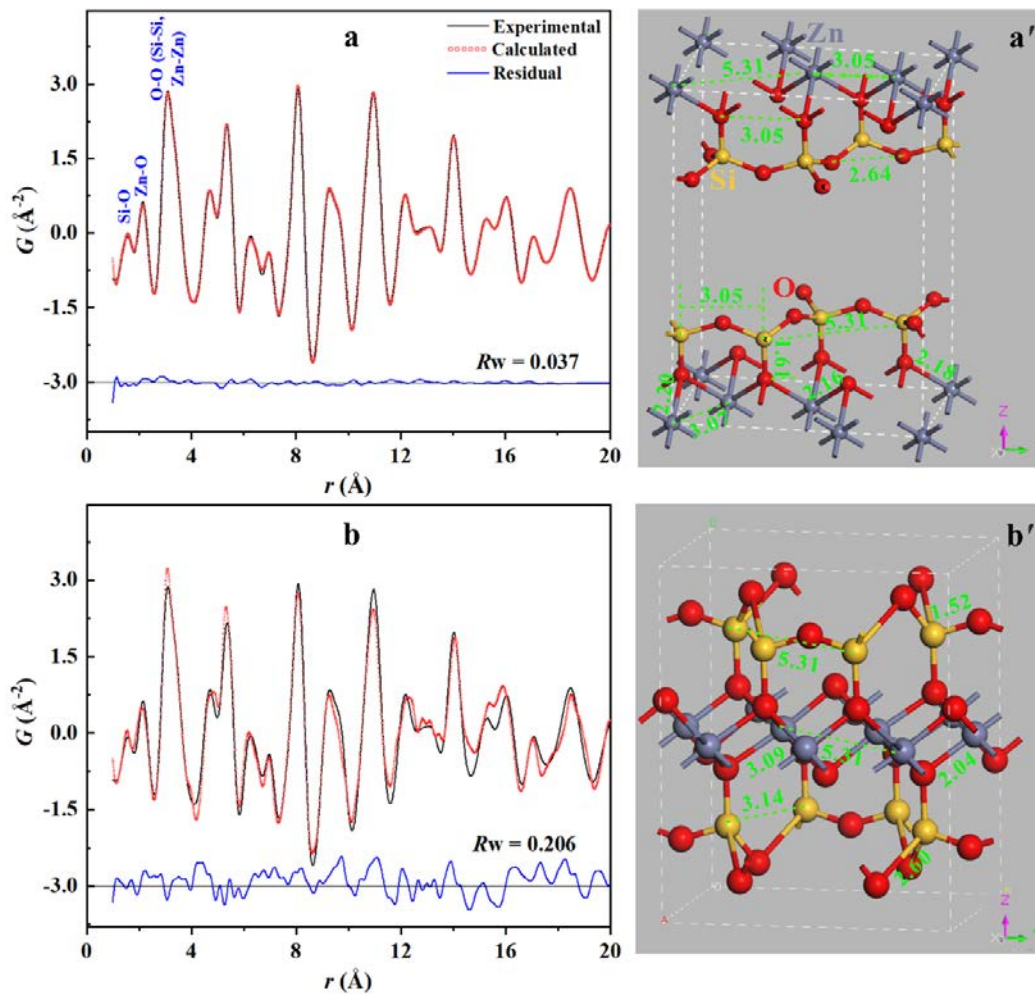838
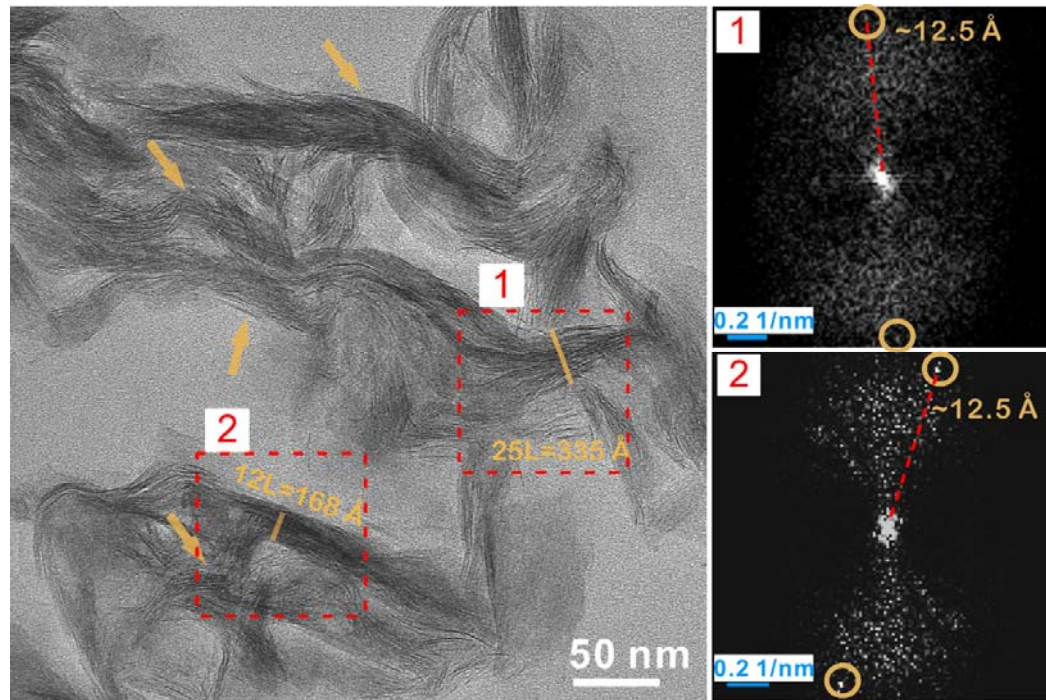
839

840 Figure 5

841

842

843   Figure 6

844

845

846 Figure 7

847

848

849

850   Figure 8

851

852

853   Figure 9

854

855

856   Figure 10

857